

Article

Stiffness Anisotropy and Micro-Mechanism of Calcareous Sand with Different Particle Breakage Ratios Subjected to Shearing Based on DEM Simulations

Yan Gao ^{1,2,*}, Ketian Sun ¹ , Quan Yuan ³ and Tiangen Shi ¹

¹ School of Earth Sciences and Engineering, Sun Yat-sen University, Zhuhai 519080, China; sunkt@mail2.sysu.edu.cn (K.S.); shitg@mail2.sysu.edu.cn (T.S.)

² Southern Marine Science and Engineering Guangdong Laboratory, Zhuhai 519080, China

³ Guangzhou Metro Design and Research Institute Co., Ltd., Guangzhou 510010, China; yuanquan@dtsjy.com

* Correspondence: gaoyan25@mail.sysu.edu.cn; Tel.: +86-159-1451-8020

Abstract: Stress-induced anisotropy in calcareous sand can cause an uneven displacement in island reef engineering. In this study, stiffness, as a quantitative indicator, is explored to reveal the stress-induced anisotropy in calcareous sand. Based on the discrete element method, the stiffness anisotropic characteristics of calcareous sand during shearing, as well as the impact of particle breakage, are investigated by numerical simulations. Both the macro and micro responses, i.e., the maximum shear modulus, contact normal, strong and weak contact normal force, and the direction of particle breakage, are explored for calcareous sand with different particle breakage ratios. The results show that calcareous sand exhibits notable anisotropy during shearing, with the maximum shear modulus in the vertical direction (deviatoric stress direction) being significantly greater than that in the horizontal direction. Moreover, the higher the particle breakage rate, the lower the stiffness and its anisotropy. The micro-mechanism results indicate that the primary particle breakage during the shearing process occurs in the vertical direction. That is, the particle breakage weakens the strong contact force in the vertical direction, leading to a redistribution of the strong contact forces from the vertical direction to other directions. This redistribution mainly manifests in a decrease in the anisotropy of contact normal and contact vector within the sample, as well as a decrease in the proportion of strong contact forces in the overall contacts. This, in turn, reduces the shear strength and stiffness of calcareous sand, particularly in the vertical direction, and results in a decrease in the maximum shear modulus and its anisotropy. The maximum reduction can be up to 50% of the original value. These insights can provide a certain theoretical support for the uneven displacement and long-term stability of calcareous sand for islands and reefs.

Keywords: calcareous sand; particle breakage; anisotropy; DEM



Citation: Gao, Y.; Sun, K.; Yuan, Q.; Shi, T. Stiffness Anisotropy and Micro-Mechanism of Calcareous Sand with Different Particle Breakage Ratios Subjected to Shearing Based on DEM Simulations. *J. Mar. Sci. Eng.* **2024**, *12*, 702. <https://doi.org/10.3390/jmse12050702>

Academic Editor: Jianhong Ye

Received: 20 March 2024

Revised: 14 April 2024

Accepted: 19 April 2024

Published: 24 April 2024



Copyright: © 2024 by the authors. Licensee MDPI, Basel, Switzerland. This article is an open access article distributed under the terms and conditions of the Creative Commons Attribution (CC BY) license (<https://creativecommons.org/licenses/by/4.0/>).

1. Introduction

In the South China Sea region, calcareous sand is widely distributed and typically chosen as the primary construction material for island and reef engineering projects [1–6]. Different from quartz sand, calcareous sand is an aggregate of insoluble carbonate minerals (mostly calcium carbonate), characterized by its irregular particle shape, high internal porosity, being easy to break, high angularity, and high internal friction angle [7–11]. Under conventional stress, particle breakage directly changes the internal structure of calcareous sand, including particle size distribution [12], packing density [13], friction angle [14], particle strength [15], permeability, and microstructure [16]. Currently, research on particle breakage is mainly based on laboratory experiments and field tests [17–20]. For example, Xiao et al. [13] found that the relationship between the particle strength and particle size of calcareous sand conforms to the Weibull distribution [21]. Coop et al. [22] discovered that under very large displacement conditions, calcareous sand reached a stable

gradation that depends on the applied normal stress and initial gradation; at the same time, particle breakage occurred and caused volume continual compression until reaching a stable gradation. Liu et al. [19] proposed that particle breakage is related to particle hardness and stress state. Yu [18] suggested that a higher confining pressure would lead to more particle breakage. Particle breakage has a significant effect on the properties of calcareous sand. However, there are still shortcomings in the current research, such as its excessive cost, discrete results, and poor process repeatability. More importantly, due to the inherent dispersion and heterogeneity of calcareous sand, microscopic understandings of particle breakage are still insufficient.

Furthermore, extensive research has been conducted on calcareous sand to investigate its strength property, considering the influences of vertical stress, relative density, and particle size distribution. Gao et al. carried out a series of indoor experiments to investigate the shear characteristics [5], creep properties [6], and the relationship between particle breakage and plasticity work [4]. Zhang et al. [23] studied the results of triaxial shear tests on calcareous sand under different confining pressures and shear strains and analyzed the influencing factors and degree of particle breakage by the Hardin model. Yan et al. [24] conducted triaxial shear tests on calcareous sand with different particle sizes, relative densities, and confining pressures and introduced the stress-induced softening coefficient and shear dilatancy coefficient to quantitatively characterize the softening and dilatancy features. However, different stress paths on particle breakage and the anisotropy of shear strength were not considered. The anisotropy of shear strength in soil has long been considered a key issue and has been included in the analysis to improve the accuracy of soil strength prediction. In addition to the inherent anisotropy formed during the deposition process of soil particles, there is also an anisotropy caused by uneven external stresses. Toyota et al. [25] studied the variation of undrained shear strength of cohesive soil in different shear directions and stress conditions through hollow cylinder torsion tests. Hwang et al. [26] used finite element simulation to study the changes in stress state caused by excavation-induced slope sliding, resulting in the anisotropy of soil strength. Coccia and McCartney [27] evaluated the effect of stress-induced anisotropy on saturated soil thermal volume change using a true triaxial test. Pan et al. [28] studied the undrained triaxial compression and tension behavior of saturated sand under different static pre-shearing conditions through experiments and analyzed the effects of pre-shearing on the anisotropy of sand elasticity, stiffness degradation, shear strength, and instability.

The different forces acting in the vertical and horizontal directions in island reef engineering, such as overlying soil pressure and building load pressure in the vertical direction and hydrostatic pressure in the horizontal direction, often lead to anisotropy of the foundation. However, for calcareous sand, research on macro- and micro-scale anisotropy with consideration of particle breakage is still in its initial stages. For example, He et al. [29] experimentally observed the pseudo-critical state, critical state, peak state, and phase transition state of calcareous sand under undrained and drained triaxial shear conditions. They studied the influence of different initial anisotropic stress states on the monotonic strength, deformation, and particle breakage characteristics of calcareous sand and found that the initial average effective stress and anisotropic stress ratio have a significant impact on the mechanical behavior of carbonate sand. However, the sieving method they used can only qualitatively evaluate the influence of particle breakage on the macroscopic properties and cannot reflect the micro-mechanism of particle breakage or reveal the influence of particle breakage on the macro/microstructure and deformation.

In recent years, the discrete element method [30] (DEM) has been proven to be a powerful tool for exploring the behavior of granular materials, such as shear strength, volume expansion, fracture evolution, contacts transmission, and energy distribution. Various DEM algorithms have been used to numerically simulate particle breakage and provide microscopic interpretations of experimental phenomena. These studies considered stress paths (e.g., confining pressure [31] and cyclic loading [32]), particle shape (e.g., particle roundness [33], sphericity [34], aspect ratio [35], particle size [36], boundary conditions [37],

and intermediate principal stress [38]), etc. In this study, a series of triaxial shear numerical simulations is conducted based on the open-source 3D discrete element platform Yade [39], studying the shear strength, deformation characteristics, stiffness, microscopic behavior, and anisotropy of calcareous sand with different particle breakage rates.

2. Methods

2.1. Details of Numerical Simulations

2.1.1. Model Parameters

A cubic shape with dimensions of $10 \times 10 \times 10 \text{ mm}^3$ was adopted into the DEM numerical model for the sample of calcareous sand. All generated particles with particle radii ranging from 0.24 to 0.48 mm are spherical in shape to avoid the anisotropy induced by internal structure. The particle gradation satisfies a uniform distribution with the average radius of 0.36 mm. The particle–particle contacts are modeled using the Hertz–Mindlin nonlinear contact model. The values of radius distribution, Young’s modulus, Poisson’s ratio, and density were determined based on the results of laboratory experiments [40], which are listed in Table 1.

Table 1. The values of the main parameters in simulations.

Parameter		Value			
Particles	Particle number	3000			
	Radius	0.24–0.48 mm			
	Density	2810 kg/m ³			
	Young’s modulus	800 Mpa			
	Poisson’s ratio	0.3			
	Internal friction angle	Sample preparation/compression: 0° Shearing: 30°			
	Degree of particle breakage	None	Low	Mid	High
	Uniaxial tensile strength (Mpa)	∞	4	2	1
	Uniaxial compressive strength (Mpa)	∞	6	6	3
	Walls	Young’s modulus	800 Mpa		
Poisson’s ratio		0.05			
Internal friction angle		Sample preparation/compression: 0° Shearing: 30°			

To examine the influence of the degree of particle breakage, four levels of particle breakage, termed as high, medium, low, and none, were used, corresponding to approximately 10%, 5%, 1%, and 0% of the particle breakage rate, which is a ratio of the number of broken particles to the total number of particles. These four terms, “high, medium, low and none”, were also consistently used in the following figures and discussion.

During the shearing process, an initial confining pressure of 400 kPa was applied, followed by maintaining a vertical strain rate of 2%/s until the vertical strain (axial strain) reached 18%, at which point the specimen was considered to be failed, and the shearing process was thereby terminated. Throughout the simulation, it was ensured that the unbalanced force rate does not exceed 0.01 to avoid unstable configurations.

2.1.2. Particle Breaking Mode

In the numerical simulations, the post-positioning method was used to simulate the particle breakage of calcareous sand. When the inter-particle contact force meets certain conditions, the particle breaks, and new particles are generated and replace the original particle. The strength criterion for determining whether the particle breaks is the modified Mohr–Coulomb–Weibull strength criterion proposed by Gladkyy [41], which uses the Mohr–Coulomb law with tensile and compressive cut-off and also considers the influence of particle size on the strength of a single particle. The relationship between

particle strength and particle size follows the Weibull distribution. The particle replacement criterion is modified from the algorithm proposed by Brzeziński [42], and the specific replacement method is illustrated in Figure 1. When a particle is broken according to the Mohr–Coulomb–Weibull strength criterion, it is replaced by several small particles with equal radii. In this study, guided by previous studies [43–45], each particle is replaced with 9 small particles with equal radii when it breaks, and the basic parameters of the new particles (e.g., density, Young’s modulus, etc.) are consistent with the original crushed particles. To ensure mass conservation before and after the breakage, the filling area was extended to the surrounding area. When the surrounding space is insufficient for successful replacement, the replacement is abandoned directly. This study optimizes the behavior when replacement fails and introduces a “delayed failure” mechanism guided by the experimental results of calcareous sand [40]. That is, when the space is limited, it is assumed to have been fractured, but the fractured particles are densely packed without replacement; when there is sufficient space later, the fractured particles are released and affect the surrounding particles, and regardless of whether they still meet the failure criteria, they are replaced.

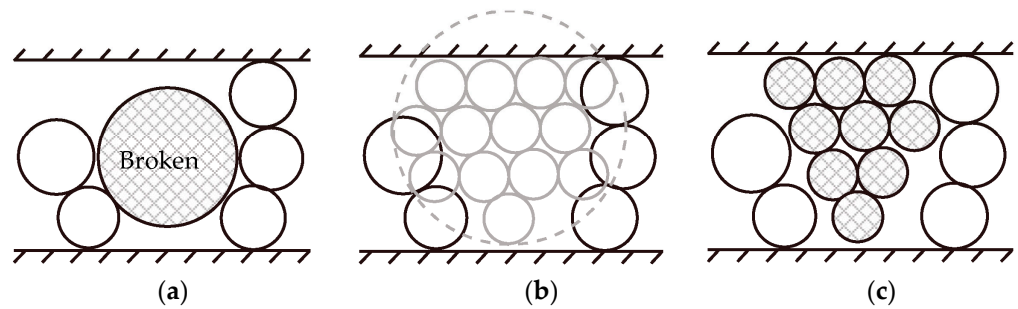


Figure 1. Spherical particle breakage mode process: (a) identify the particles to be crushed; (b) search for the potential locations of daughter particles; (c) fill when the daughter particles can be packed to a predetermined amount (modified from Gladky [41]).

2.1.3. The Maximum Shear Modulus, G_{max}

The anisotropy of soil properties is primarily attributed to two main factors: internal and external causes. The former arises from the irregular shape of the particles, while the latter results from uneven external loads. In this study, spherical particles were used; thus, the anisotropy generated by the particles themselves can be neglected, and the anisotropy generated during the shearing process is mainly caused by external loads. To characterize the anisotropy of calcareous sand during shearing, the shear modulus was used as an indicator. It is well known that the shear modulus itself decreases with increasing shearing strain, while it is almost constant when the shearing strain is very small ($<10^{-6}$ for sand), which corresponds to the maximum shear modulus G_{max} . Hence, the maximum shear modulus G_{max} is used to describe the anisotropic behavior of calcareous sand. In order to obtain G_{max} values at different shearing levels, the sample is first sheared to the target state by the triaxial test simulation (corresponding to different axial strains); then, another simple shearing mode is conducted, as shown in Figure 2. Since the shearing strain during the simple shearing process is very small ($<10^{-6}$) and the internal structure cannot be changed, the obtained G_{max} can represent the level of stiffness at different axial strains. As shown in Figure 2, the G_{max} of three orthogonal directions is denoted as G_{xz} , G_{yz} , and G_{xy} , respectively. Herein, x , y , and z represent three mutually perpendicular directions. By using G_{xz} as an example, the maximum shear modulus on the z – x plane can be determined by Equation (1):

$$G_{zx} = \frac{\tau_{zx}}{(\delta_{zx}/d_{zx})} \tag{1}$$

where τ_{zx} represents the shear stress on the z - x plane; δ_{zx} represents the lateral displacement between two walls' z -axes; and d_{zx} represents the sample dimension. This calculation method has been verified in previous studies [46].

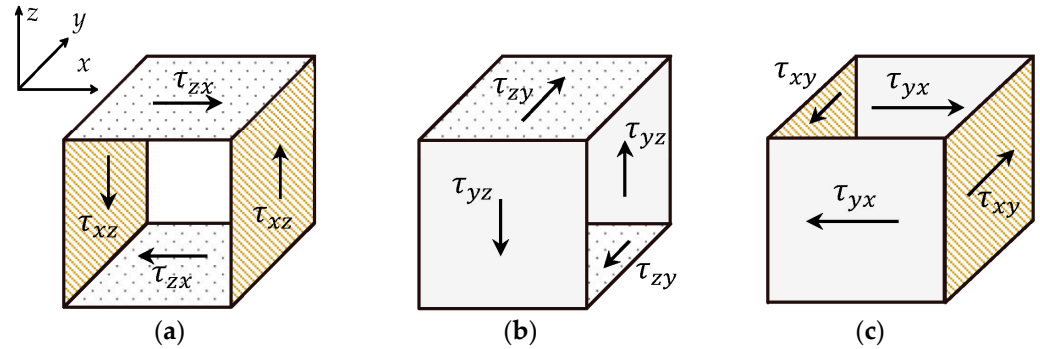


Figure 2. Shear modulus in different directions: (a) shear mode 1 G_{xz} ; (b) shear mode 2 G_{yz} ; and (c) shear mode 3 G_{xy} .

According to previous studies [47–51], in the elastic condition, the maximum shear modulus G_{max} is only related to the stress in the corresponding plane, i.e., G_{xy} is only controlled by the stress in the xy plane and is independent of the stress in the z direction.

2.2. Methodology for Micro-Scale Parameters

Guided by Radjai et al. [52], the contacts between particles are classified into two parts: strong contact normal force chain, where the contact normal force is greater than the average force, and weak contact normal force chain. These two types of contacts form two complementary networks with different geometric and mechanical properties. The strong contact normal force chain bears the entire additional stress generated by triaxial shearing, while the weak contact normal force chain only contributes to maintaining the average stress. To explore the intrinsic mechanisms of the anisotropic characteristics during the shearing of calcareous sand, the evolutions of microscopic parameters, such as the contact normal, contact vectors and their directions, the magnitude of contact normal forces, and the direction of particle breakage, were analyzed.

2.2.1. Anisotropy of Contact Normal

The contact normal force direction between two adjacent particles, known as the contact normal, refers to the direction perpendicular to the contact surface. To quantitatively characterize the anisotropy degree of contact normal, the fabric tensor of microstructures [53] was introduced as follows:

$$N = \frac{1}{N_c} \sum_{c=1}^{N_c} (n^c \otimes n^c) \tag{2}$$

where n^c is the unit vector of contact normal and N_c is the number of contacts between particles. The eigenvalues and eigenvectors of the fabric tensor can reflect the concentration of anisotropy of the contact normal and principal directions. The coefficient of anisotropy is given as follows:

$$\Delta\Phi = \sqrt{\frac{(e_1^N - e_2^N)^2 + (e_2^N - e_3^N)^2 + (e_1^N - e_3^N)^2}{2}} \tag{3}$$

where e_i^N ($i = 1, 2, \text{ or } 3$) represents the three eigenvalues of the fabric tensor N . At the same time, selecting the eigenvector corresponding to the maximum eigenvalue represents the dominant direction of anisotropy.

2.2.2. Anisotropy of Contact Vector

The contact vector is the vector connecting the centroids of two contacting particles. The branch tensor can reflect the average length of the line connecting the centroids in different directions in space, equivalent to the average radius of the contacting particles. The higher the contact vector, the larger the related particles. In order to distinguish the anisotropy of the contact vector from the anisotropy of the contact direction, the formula proposed by Sitharam et al. [54] was used to calculate the contact vector tensor B^n :

$$B_{ij}^n = \frac{1}{N_c} \sum_{c=1}^{N_c} \frac{l_c^n n_i^c n_j^c}{E(n^c)_{ij}} \tag{4}$$

where n^c represents the contact normal; l_c^n is the length of the contact vector, defined as the distance between the centroids of two contacted particles; and $E(n)$ is the probability density function of the contact normal. For any direction vector n :

$$E(n) = \frac{1}{4\pi} \left(1 + D \odot (n \otimes n) \right) \tag{5}$$

in which D is the skew tensor of the fabric tensor N shown in Equation (2). On this basis, to conveniently compare the anisotropy degree under different axial strains, the normalized contact vector tensor $B^{n'} = B^n \odot \frac{1}{tr(B^n)}$ was used to calculate the level of anisotropy. The calculation method for the coefficient of anisotropy for the contact vector $\Delta\Phi_{cv}$ is consistent with the form of $\Delta\Phi$ for the contact normal (Equation (3)), where e_i ($i = 1, 2, \text{ or } 3$) represents the three eigenvalues of the contact vector tensor. The dominant direction is also represented by the related eigenvector corresponding to the maximum eigenvalue.

2.2.3. Anisotropy of Contact Normal Force

The external load is mainly borne by the contact normal force between particles, which is the component of the contact force between two particles along the normal direction. The formula defined by Sitharam [54] was also used for this calculation. The normalized degree of anisotropy $\Delta\Phi_{cf}$ was also used to facilitate the comparison of the anisotropy of contact normal force magnitudes under different axial strains, and the related eigenvector corresponding to the maximum eigenvalue also represents the dominant direction. For all contact normal force vectors, the contact normal force is demoted as f_c^n . The specific formula for calculating the contact normal force tensor is as follows:

$$\begin{cases} F_{ij}^n = \frac{1}{N_c} \sum_{c=1}^{N_c} \frac{f_c^n n_i^c n_j^c}{E(n^c)_{ij}} \\ F^{n'} = F^n \odot \frac{1}{tr(F^n)} \end{cases} \tag{6}$$

where $E(n)$ is the probability density function of the contact normal.

2.2.4. Quantification of Particle Breakage Direction Anisotropy

To further explore the influence of particle breakage on the anisotropy of inter-particle contacts, the degree of anisotropy and the principal direction of particle breakage were studied. The direction of maximum contact normal force during particle breakage was taken as the direction of particle breakage. Given the particle breakage direction vector n^b and the related contact number N_b , the particle breakage tensor N^b was determined as follows:

$$N^b = \frac{1}{N_b} \sum_{b=1}^{N_b} \left(n^b \otimes n^b \right) \tag{7}$$

The calculation of the degree of anisotropy and the principal direction were similar to that for the contact normal detailed in Section 2.2.1. The degree of anisotropy $\Delta\Phi_{pb}$

was calculated using the eigenvalues of N^b substituted into Equation (3). The principal direction of anisotropy was determined using the eigenvector corresponding to the maximum eigenvalue.

3. Results

3.1. Shear Characteristics and Stiffness Variation of Calcareous Sand with Different Particle Breakage Rates

3.1.1. Stress–Strain Relationship

As shown in Figure 3, the shear stress–strain response of calcareous sand increases rapidly in the initial stage (axial strain less than 3%), and the curves are basically overlapped for different particle breakage ratios. This is because the shear deformation in this stage is mainly controlled by the adjustment of particle positions caused by particle rotation and sliding and the filling of internal large voids, accompanied by insignificant particle crushing (Figure 4). As the deviatoric stress continues to increase, the stress–strain relationships of calcareous sand with different particle breakage ratios show differences: the deviatoric stress of calcareous sand with a higher particle breakage ratio is obviously lower than that with a lower particle breakage ratio at the same axial strain. More stress drops occur for calcareous sand with a higher particle breakage ratio during shearing, which is caused by the stress release induced by particle crushing.

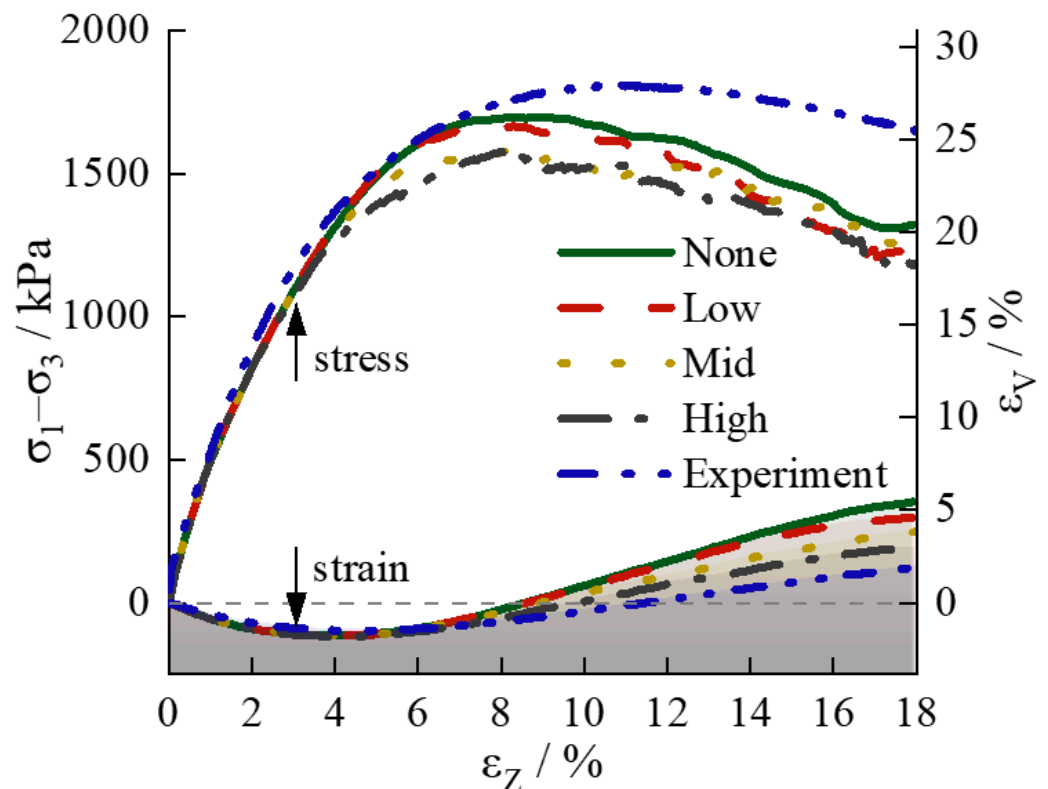


Figure 3. Deviatoric stress–axial strain and volume strain–axial strain curves for calcareous sand with different particle breakage rates.

The volume change during the shearing is the first contraction, followed by dilation. When the axial strain is less than 6%, the volumetric strain–axial strain curves of the calcareous sand with different particle breakage ratios are basically overlapped because, before this point, the overall particle breakage is at a relatively low level and changes little (Figure 4). With the increase in axial strain, the level of particle breakage increases. As shown in Figure 4, for the calcareous sand with a higher degree of particle breakage, particle breakage occurs earlier, and the rate of particle breakage growth is also faster. The

continual increase in particle breakage makes the dilation tendency of the calcareous sand decrease even further.

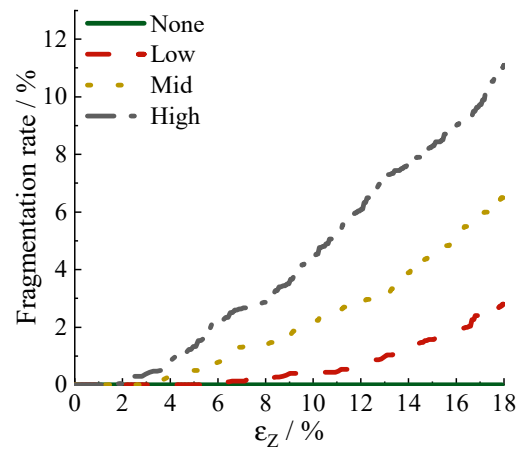


Figure 4. The variation in the particle breakage rate with axial strain for different calcareous sands.

These simulation results are consistent with previous studies (e.g., reference [55]) and laboratory experiments. There are discrepancies between the current simulation results and the experimental results at large strains, specifically manifested as a significant overestimation of volume dilation and an underestimation of peak stress, as shown in Figure 3. The possible reason is the lack of consideration of the actual particle shape, surface roughness, intra-particle voids, and so on. However, it is believed that the tendency of the current results is accurate for studying the causes of stress-induced anisotropy.

3.1.2. Macroscopic Stiffness Anisotropy

During shearing, as the axial strain increases, the changes in G_{xz} , G_{yz} , and G_{xy} are shown in Figure 5. For different particle breakage rates, with the increase in axial strain, both G_{xz} and G_{yz} first increase to a peak until the axial strain reaches 4–5% and then decrease. Meanwhile, G_{xy} remains basically unchanged until reaching the 2% axial strain and then decreases. This is because with the increase in axial strain, the stress in the z direction increases, while the stresses in the x and y directions remain unchanged. The maximum shear modulus in the elastic condition is only related to the stress in the shear plane. However, after reaching a certain level of strain, the specimen begins to exhibit plastic deformation, and the original structure of the calcareous sand is destroyed. Therefore, the maximum shear moduli in all directions decrease. Based on Figure 5, it can also be observed that at low axial strains (<2%), the maximum shear modulus G_{max} for different particle breakage rates basically overlaps as before this point, the degree of particle breakage is low and the influence of particle breakage on the macroscopic stiffness of the specimen is not significant. As the axial strain increases, with the particle breakage increasing, the level of increase in G_{max} decreases more for samples with higher particle breakage. At large axial strains (>6%), the higher the particle breakage rate, the smaller the G_{max} value. In other words, particle breakage weakens the stiffness of calcareous sand, and the reduction can be up to 50% compared with that without particle breakage, which is crucial for the stability and safety assessments of the foundations of calcareous sand.

The maximum shear moduli in different directions have different magnitudes and trends, showing significant anisotropy. The changes in G_{xz}/G_{yz} and G_{xz}/G_{xy} with the axial strain are shown in Figure 6 and Table 2. Throughout the entire shearing process, G_{xz}/G_{yz} is close to one, and G_{xz}/G_{xy} continually increases. There is a significant difference in the maximum shear moduli between the horizontal and vertical planes; that is, the stiffness in the vertical direction is greater than that in the horizontal direction during shearing. With the increase in axial strain, the degree of anisotropy increases. As the particle breakage rate increases, the ratio of G_{xz}/G_{yz} under the same axial stress does not change significantly

at small strains, but at higher strains, it is much lower under higher particle breakage rates. That is, particle breakage can induce the macroscopic stiffness and related degree of anisotropy of the calcareous sand decrease, and the degree of decrease is related to the particle breakage rate; the larger the rate, the greater the decrease.

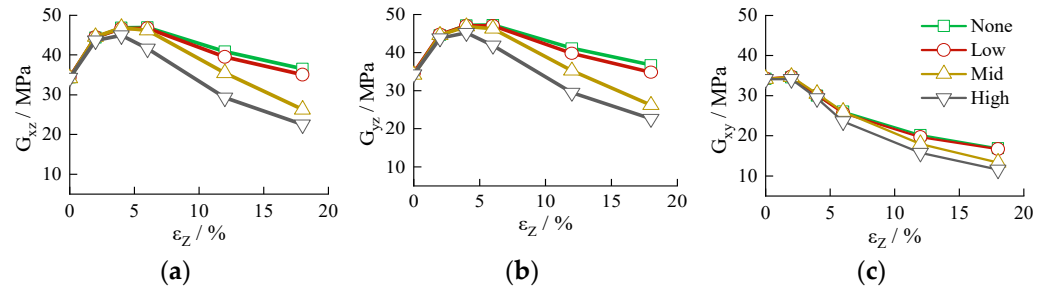


Figure 5. The evolution of small-strain shear moduli in different directions as the axial strain increases during the shearing process: (a) G_{xz} ; (b) G_{yz} ; and (c) G_{xy} .

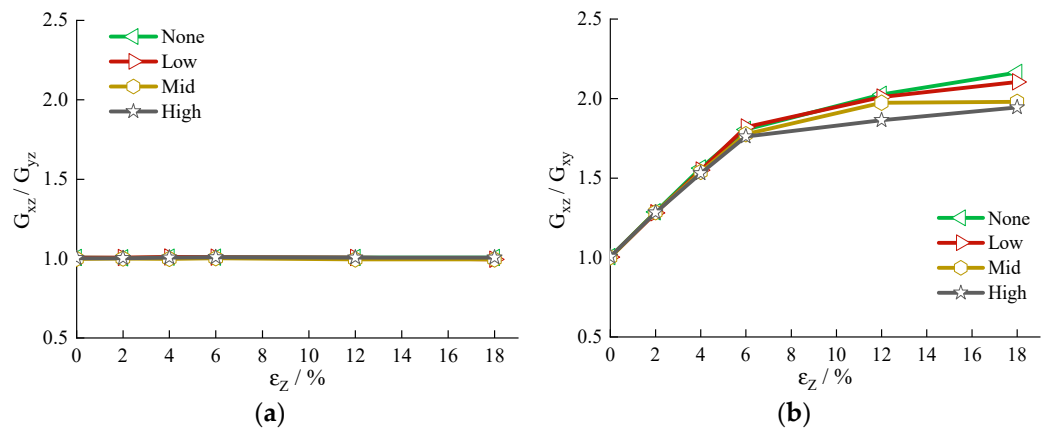


Figure 6. The difference in small-strain shear moduli in different directions during shearing with increasing axial strain: (a) G_{xz}/G_{yz} and (b) G_{xz}/G_{xy} .

Table 2. Variation in G_{xz}/G_{xy} for calcareous sand with different particle breakages.

Strain (%)	None	Low	Mid	High
0	1.004	1.003	1.001	1.004
2	1.286	1.281	1.285	1.282
4	1.562	1.550	1.539	1.529
6	1.805	1.821	1.775	1.761
12	2.025	2.009	1.974	1.860
18	2.163	2.103	1.979	1.944

3.2. Anisotropy of Internal Contact Forces

During shearing, the external stress causes different responses in the contact normal forces between the calcareous sand particles. As shown in Figure 7, taking the situation under the 18% axial strain as an example, the magnitudes of the contact forces between the particles in the horizontal direction (XOY plane) and the vertical direction (XOZ plane) are significantly different. In the XOY plane, the magnitude of the contact forces does not have a clear dominant direction. It is consistent in all directions, forming a circular distribution of force magnitudes. In the XOZ plane, the magnitude of the contact forces forms an elliptical distribution, with the contact forces in the Z direction being significantly greater than those in the X direction, consistent with the larger external stress in the vertical direction. The internal microstructural features can reflect macroscopic phenomena.

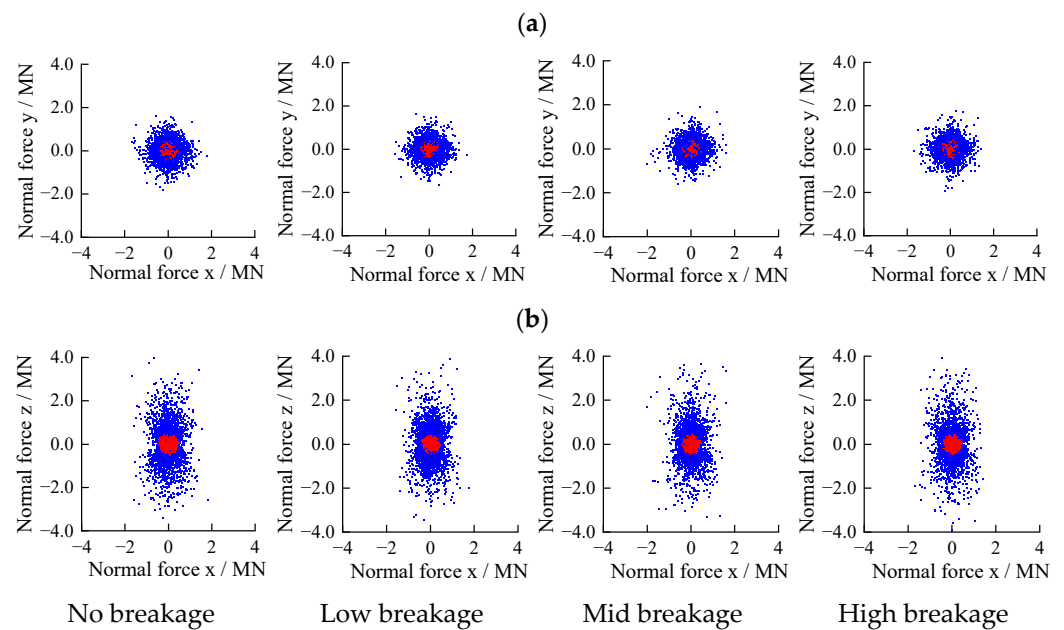


Figure 7. Projection of inter-particle contact forces in calcareous sand at different planes under an 18% axial strain: (a) XOY plane and (b) XOZ plane. In this figure, the blue points represent strong contact forces, and the red points represent weak contact forces.

4. Discussion

Macroscopic behavior can be reflected and related to the internal structure’s evolution. Based on the relationship between the stress and strain for calcareous sand during shearing (Figure 3), two representative cases of particle breakage rate, including no particle breakage and high particle breakage, and three axial strains at 2% (before the peak deviatoric stress), 6% (around the peak deviatoric stress), and 18% (after the peak deviatoric stress) are selected for comparison. The indicators of internal structure for calcareous sand, i.e., contact normal, contact vector, distribution of contact normal forces, and the direction of particle breakage, are discussed.

4.1. Contact Normal

4.1.1. Distribution of Contact Normal

The projections of contact normal in the XOY and XOZ planes are shown by the density proportional rose diagrams in Figures 8 and 9, respectively. In the XOY plane, there is no significant preferential direction for both strong and weak contacts, and the distribution of contact normal is circular, with a significantly larger number of weak contacts than strong contacts. In the XOZ plane, there is a clear preferential direction for strong and weak contacts, mainly distributed in the vertical direction (Z direction) for strong contacts and in the horizontal direction (X direction) for weak contacts. Furthermore, with the increase in axial strain, the number of weak contacts in the horizontal direction significantly decreases.

The direction of maximum contact normal force for particle breakage is served as the direction of particle breakage [44,56], which is also shown in Figure 9. There is no significantly preferred direction for particle breakage in the XOY plane, but in the XOZ plane, particle breakage mainly occurs in the vertical direction (Z direction), indicating the existence of anisotropy in particle breakage. Under the same axial strain, the comparison of the samples with high particle breakage and without particle breakage is shown in Figure 10 (i.e., Figures 8 and 9). It is clearly seen that the particle breakage level reduces the strong contact, especially in the Z direction, while the weak contact increases in the Z direction. In other words, particle breakage effectively reduces the concentration of strong contact forces in the Z direction, thereby reducing the degree of anisotropy.

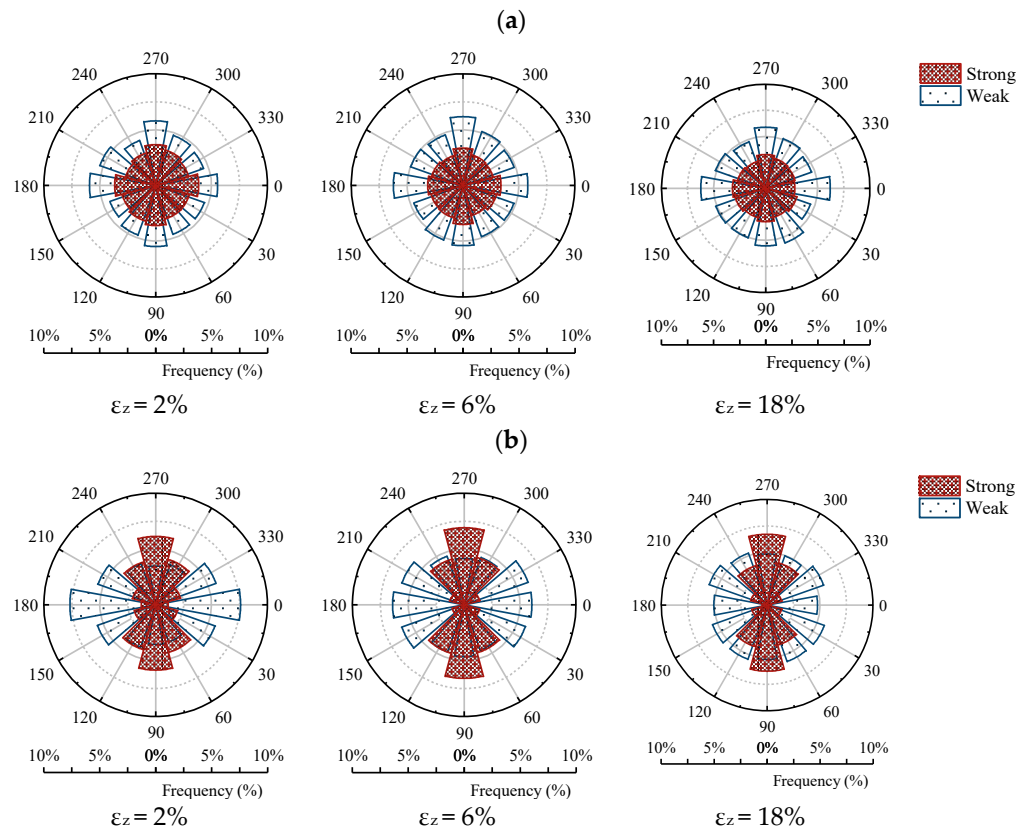


Figure 8. Distribution of inter-particle contact normal under different axial strains without particle breakage: (a) XOY plane and (b) XOZ plane.

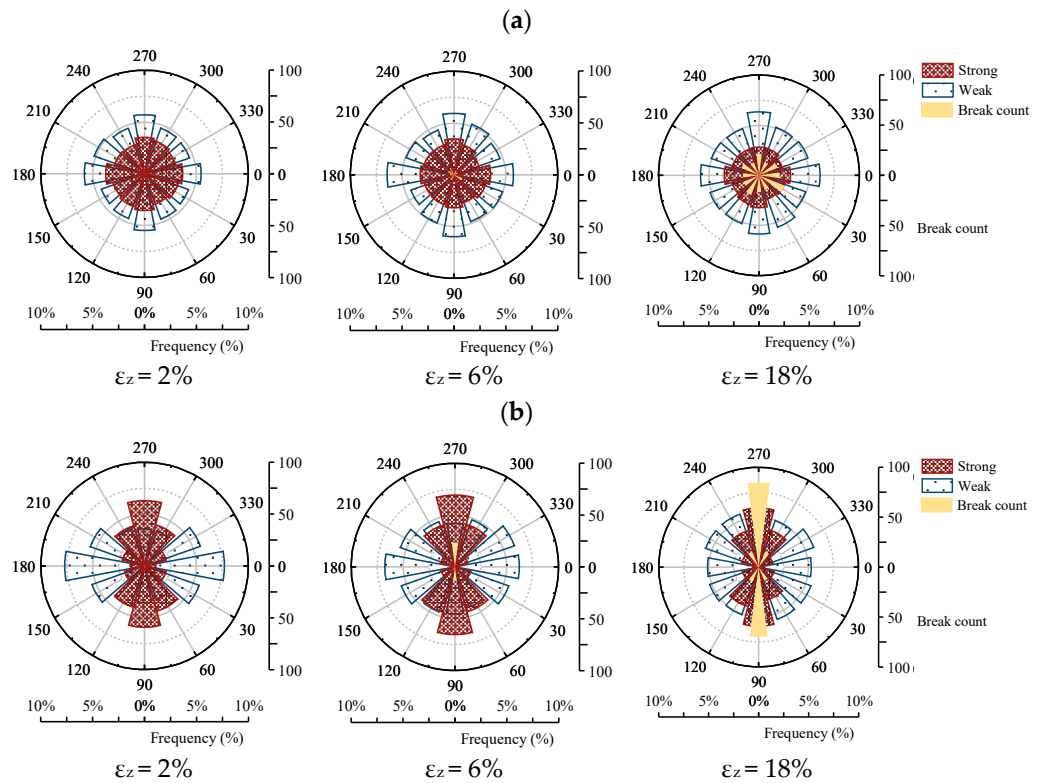


Figure 9. Distribution of inter-particle contact normal under different axial strains at high particle breakage rates: (a) XOY plane and (b) XOZ plane.

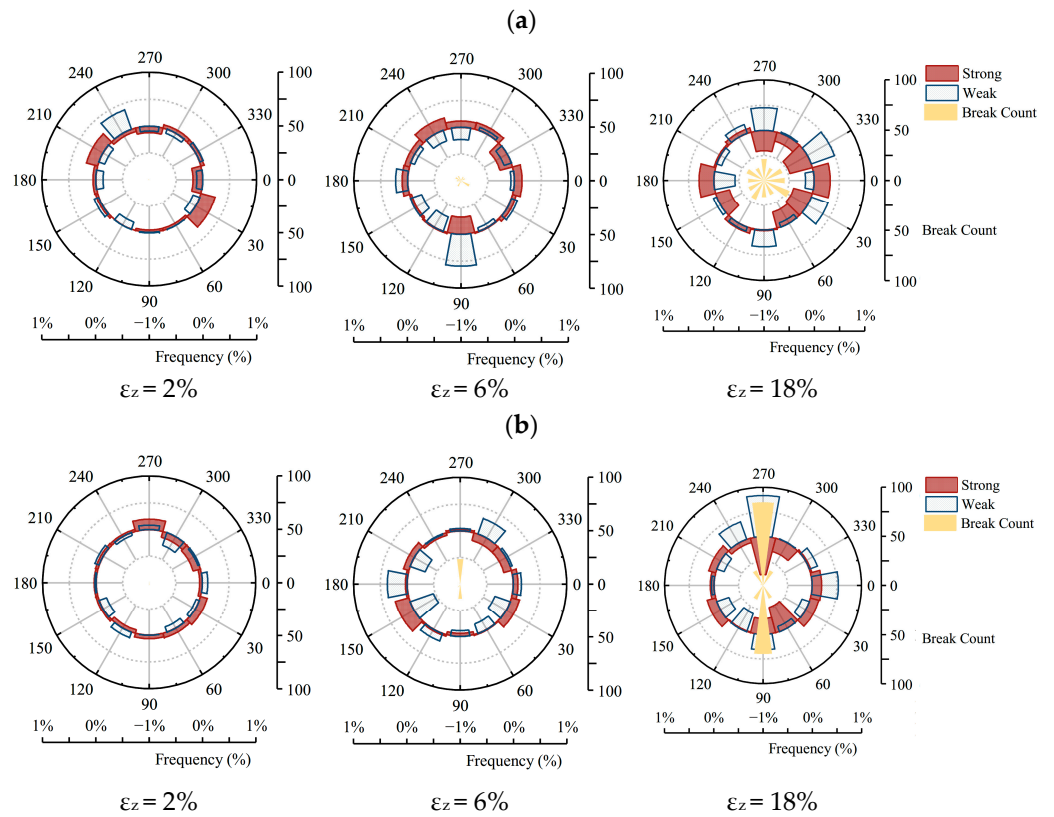


Figure 10. Influence of particle breakage on the distribution of inter-particle contact normal at different axial strains: (a) XOY plane and (b) XOZ plan.

4.1.2. Contact Normal Anisotropy

Figure 11 shows the anisotropy degree of the orientation of strong and weak contacts (represented by the fabric tensor) during the shearing process as a function of axial strain, where N, L, M, and H represent no, low, medium, and high particle breakage, and S and W denote strong and weak contacts, respectively. These symbols have the same meanings as in the following figures. Throughout the entire shearing process, the dominant direction of the strong contacts is consistently in the vertical direction ($\sim 90^\circ$; Z direction in Figure 11a), while the dominant direction of the weak contacts is in the horizontal direction (0° ; X or Y direction in Figure 11a), with occasional fluctuations affected by particle breakage.

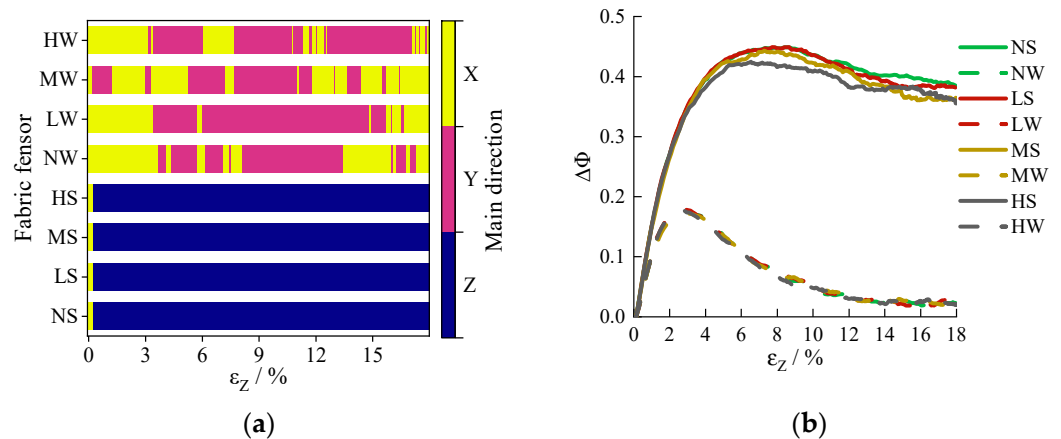


Figure 11. Anisotropy of particle contact orientation (fabric tensor) for different particle breakage ratios: (a) dominant direction and (b) anisotropy degree.

For weak contacts, with the increase in axial strain, the degree of anisotropy first increases, reaching its maximum value at around a 3% axial strain, and then significantly decreases to negligible levels. This variation reflects the transition of deformation in the calcareous sand from elastic to plastic deformation during shearing. The degree of anisotropy coefficients at different particle breakage rates are similar and much smaller than the anisotropy of strong contacts. This indicates that particle breakage has almost no effect on the anisotropy of weakly bonded particles.

For strong contacts, the maximum level of anisotropy appears at around 6–12% axial strain and then decreases slightly. For different particle breakage rates, there is no significant difference in the initial shear stage. The degree of anisotropy for the higher particle breakage rate of calcareous sand is significantly smaller when the axial strain exceeds 3%. It proves that particle breakage can affect the anisotropy of the strong contacts. The higher the particle breakage rate, the lower the degree of anisotropy. Due to the strong contacts controlling the overall strength and stability of calcareous sand [57,58], one of the intrinsic reasons for the reduction in the macroscopic anisotropy degree (e.g., the maximum shear modulus, as shown in Figure 4) is the reduction in the anisotropy of the strong contacts between particles.

4.2. Contact Vector Anisotropy

During shearing, the anisotropy degree of the strong contact vector with respect to the axial strain development is shown in Figure 12. Similar to the results of the contact normal, the dominant direction of the strong contact vector is always in the vertical direction ($\sim 90^\circ$), and the dominant direction of the weak contact vector is mainly in the horizontal direction (0°), but it fluctuates occasionally due to particle breakage. Particle breakage has almost no effect on the anisotropy magnitude of the weak contact vector. For strong contacts, after the 6% axial strain, with the increase in axial strain and particle breakage rate, the degree of anisotropy decreases, but the difference is not significant. That is, the higher the particle breakage rate, the lower the anisotropy degree of the contact vector, but the impact is weak. It is also indicated that the strong contacts in the Z direction is mainly borne by large particles. This is because the preferred direction of the contact vector for strong contacts is along the Z direction, and the corresponding anisotropy of the contact vector tensor $B^{n'}$ is higher. This suggests that the average radius of the particles bearing strong contacts in the Z direction is larger. As the particle breakage rate increases, there is a slight decrease in the $\Delta\Phi_{cv}$ for strong contacts, whereas the $\Delta\Phi_{cv}$ for weak contacts remains relatively unchanged, which indicates that particle breakage is likely to occur more frequently in the larger particles that bear strong contacts. The reduced anisotropy of the contact vector of the strong contacts means that the size of the particles bearing the strong contacts along the Z direction decreases.

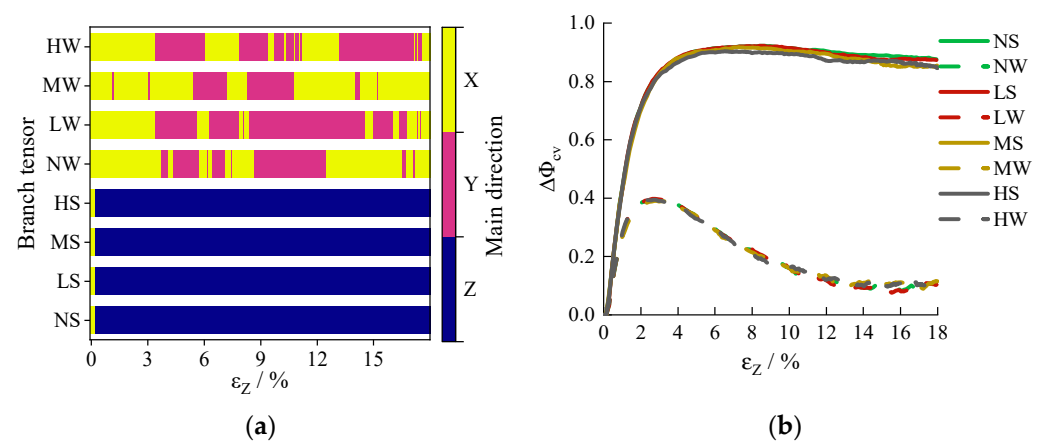


Figure 12. Anisotropy of contact branch vectors at different particle breakage rates: (a) dominant direction and (b) anisotropy degree.

4.3. Contact Normal Force

4.3.1. The Anisotropy of Contact Normal Forces

The normalized anisotropy degree and principal direction of the contact normal forces are shown in Figure 13. It is readily seen that no significant changes are obtained under different particle breakage rates. That is, particle breakage does not have a considerable influence on the contact normal forces in terms of the anisotropy degree and principal direction.

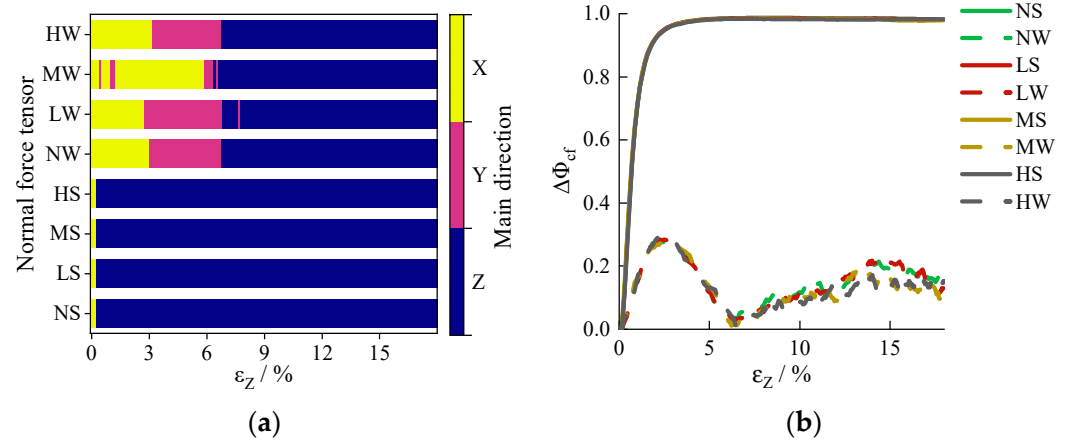


Figure 13. Anisotropy of normal contact forces in the strong and weak contacts at different particle breakage ratios: (a) dominant orientation and (b) anisotropy degree.

4.3.2. The Distribution of Contact Normal Forces

Taking the representatives at the axial strains of 2%, 6%, and 18% of calcareous sand with no particle breakage and high particle breakage, the contact normal force distribution histograms are shown in Figure 14. Under a small axial strain, the contact normal force distributions are almost identical due to the insignificant particle breakage for calcareous sand with different particle breakage rates. As the shearing progresses, the number of strong contact normal forces of calcareous sand with high particle breakage is significantly smaller than that with no particle breakage, while the number of weak contact normal forces is significantly larger. The evolution of the percentage of weak contacts during shearing in Figure 15 also indicates a decrease in the proportion of strong contact normal forces and an increase in the proportion of weak contact normal forces. At the same time, the increase in weak contact normal forces in calcareous sand with high particle breakage is significantly greater than in calcareous sand with no particle breakage. In other words, particle breakage can enlarge the destruction of strong contacts and the formation of weak contacts between particles in calcareous sand.

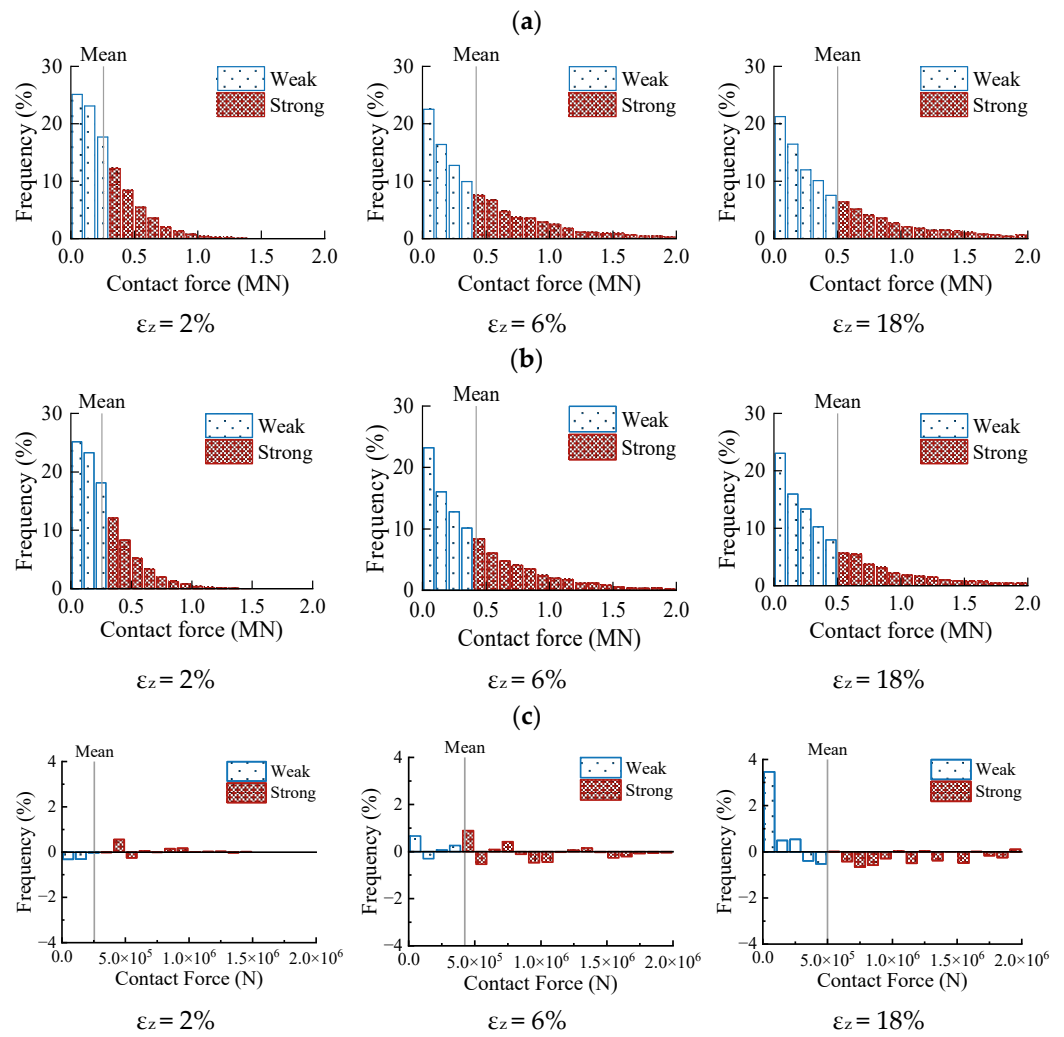


Figure 14. Influence of particle breakage on contact normal force distributions at different axial strains for calcareous sand with different particle breakage rates: (a) no particle breakage; (b) high particle breakage; and (c) variation (high breakage–no breakage).

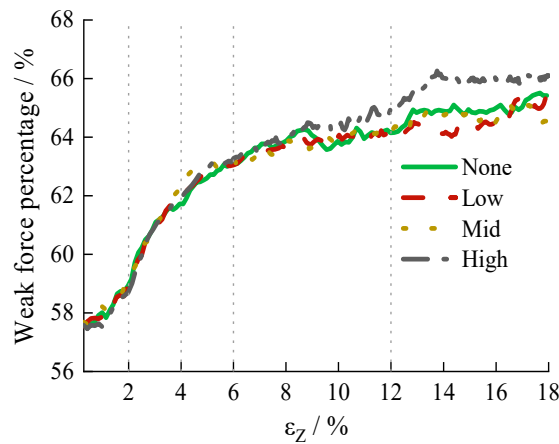


Figure 15. The variation in the proportion of weak contact normal forces with axial strain.

4.4. Anisotropy of Particle Breakage Direction

Figure 16 shows the degree of anisotropy of particle breakage and the principal direction. The principal direction of particle breakage of calcareous sand with different

degrees of particle breakage is always the vertical direction, consistent with the external deviatoric stress direction. During shearing, with the increase in axial strain, especially after the peak stress (corresponding to a 6% axial strain), the degree of anisotropy of particle breakage decreases. This is because at lower strains, only strong contacts that are nearly parallel to the Z-axis can satisfy the failure criteria. Therefore, it is considered that the direction of particle breakage is more concentrated in the direction parallel to the Z-axis at lower strains. As the strain progresses, a large number of strong contacts parallel to the Z-axis have already been extensively damaged by particle breakage. Therefore, contacts with a certain angle to the Z-axis can also satisfy the failure criteria. As a result, the level of anisotropy in the direction of particle breakage decreases. Furthermore, the greater the degree of particle breakage, the greater the reduction in the degree of anisotropy. The reduction in the degree of anisotropy of particle breakage will also lead to a decrease in the macroscopic degree of anisotropy of calcareous sand.

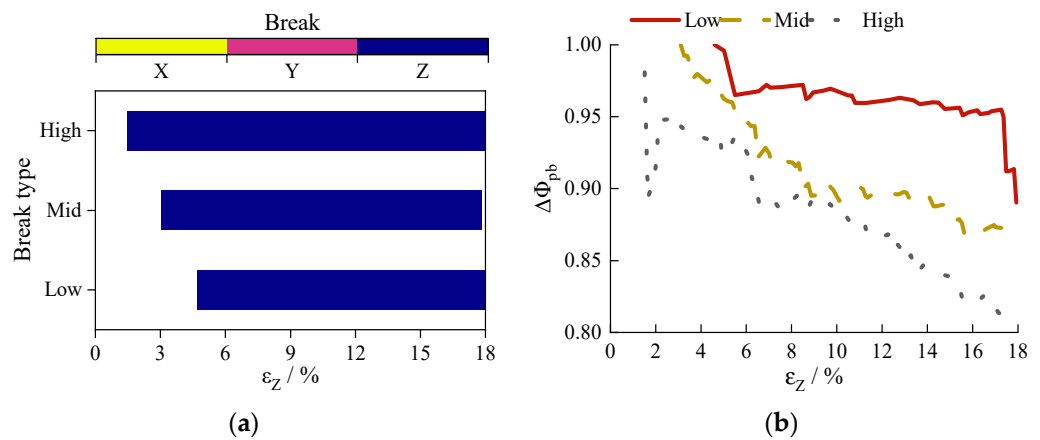


Figure 16. Anisotropy of particle breakage: (a) dominant direction and (b) anisotropy degree.

The findings of this study emphasize the importance of understanding the influence of particle breakage on the stiffness anisotropy of calcareous sand. It should be noted that the DEM method has certain limitations, such as the demand for computational efficiency and resources, along with the influence of size effects, and the increase in particle quantity due to particle breakage further slows down its computational speed. The results of this study can be used as a reference and guide for future engineering endeavors. In the future, further numerical simulations under conditions more akin to actual engineering environments could be required, considering the dynamic wave loads, the true shapes of calcareous sand particles, and more realistic forms of particle breakage, as well as variations in Young’s modulus, Poisson’s ratio, and so on. These simulations should be combined with field testing or laboratory experiments, which can enhance the reliability and application of research outcomes in practical engineering.

5. Conclusions

This study simulates the particle breakage behavior using the post-positioning method and the “delayed replacement” mechanism. The anisotropic characteristics and micro-mechanisms of calcareous sand with different particle breakage rates subjected to shearing are investigated using the discrete element numerical simulations. The main conclusions are as follows:

(1) During shearing, the macroscopic stiffness G_{max} of the calcareous sand is greater in the vertical direction than that in the horizontal direction, and the degree of stiffness anisotropy increases with the increase in axial strain. A distinct anisotropy is found. Particle breakage can reduce the stiffness in different directions, mainly in the direction of deviatoric stress, which, in turn, weakens the anisotropy characteristics of the calcareous sand induced

by external stress. As the particle breakage rate increases, the peak and residual shear stress and shear dilatancy of the calcareous sand decrease.

(2) The micro-anisotropy of the calcareous sand during shearing is mainly manifested in the distribution of contact normal directions, contact vectors, and contact normal force values between particles. During the shearing process, the strong contacts and related contact normal forces in the vertical direction are significantly greater than those in the horizontal direction, while the weak contacts and related contact normal forces in the horizontal direction are significantly greater than those in the vertical direction. Thus, particle breakages mainly occur in the vertical direction. The degree of anisotropy of particle breakage decreases with an increase in the particle breakage rate. Although particle breakage has no significant impact on the anisotropy of the contact normal force mean value and the principal direction, it mainly affects the distribution characteristics of contact normal forces. The strong contact forces decrease while the weak contact forces increase, which leads to a tendency of contact force redistribution and uniformity. The reducing strong contact normal forces results in a significant reduction in G_{max} . Additionally, the degree of anisotropy of the strong contact direction also decreases with the increase in particle breakage, thus reducing the degree of stiffness anisotropy.

Author Contributions: Conceptualization, K.S.; Methodology, Y.G.; Software, K.S.; Validation, Y.G. and Q.Y.; Formal analysis, K.S.; Investigation, Y.G.; Resources, Y.G.; Data curation, K.S.; Writing—original draft, K.S.; Writing—review & editing, Y.G., Q.Y. and T.S.; Supervision, Y.G.; Project administration, Y.G.; Funding acquisition, Y.G. All authors have read and agreed to the published version of the manuscript.

Funding: This research was supported by the National Natural Science Foundation of China (42072295), the Guangdong project (2017ZT07Z066), and the National Key R&D Program of China (2022YFC3005203). The third author, Quan Yuan, also acknowledges the support from the Guangdong Provincial Key Laboratory of New Construction Technology for Urban Rail Transit Engineering (2017B030302009).

Institutional Review Board Statement: Not applicable.

Informed Consent Statement: Not applicable.

Data Availability Statement: Data are contained within the article.

Conflicts of Interest: Author Quan Yuan was employed by the company Guangzhou Metro Design and Research Institute Co., Ltd. The remaining authors declare that the research was conducted in the absence of any commercial or financial relationships that could be construed as a potential conflict of interest.

References

- Da, B.; Yu, H.; Ma, H.; Tan, Y.; Mi, R.; Dou, X. Experimental Investigation of Whole Stress-Strain Curves of Coral Concrete. *Constr. Build. Mater.* **2016**, *122*, 81–89. [[CrossRef](#)]
- Kuang, D.; Long, Z.; Guo, R.; Zhao, T.; Wu, K. Experimental and Numerical Study on the Fragmentation Mechanism of a Single Calcareous Sand Particle under Normal Compression. *Bull. Eng. Geol. Environ.* **2021**, *80*, 2875–2888. [[CrossRef](#)]
- Xiong, H.; Qiu, Y.; Liu, J.; Yin, Z.-Y.; Chen, X. Macro–Microscopic Mechanism of Suffusion in Calcareous Sand under Tidal Fluctuations by Coupled CFD-DEM. *Comput. Geotech.* **2023**, *162*, 105676. [[CrossRef](#)]
- Gao, R.; Ye, J. Mechanical Behaviors of Coral Sand and Relationship between Particle Breakage and Plastic Work. *Eng. Geol.* **2023**, *316*, 107063. [[CrossRef](#)]
- Gao, R.; Ye, J. A Novel Relationship between Elastic Modulus and Void Ratio Associated with Principal Stress for Coral Calcareous Sand. *J. Rock Mech. Geotech. Eng.* **2024**, *16*, 1033–1048. [[CrossRef](#)]
- Ye, J.; Haiyilati, Y.; Cao, M.; Zuo, D.; Chai, X. Creep Characteristics of Calcareous Coral Sand in the South China Sea. *ACTA Geotech.* **2022**, *17*, 5133–5155. [[CrossRef](#)]
- Chen, H.Y.; Wang, R.; Li, J.G.; Zhang, J.M. Grain Shape Analysis of Calcareous Soil. *Rock Soil Mech.* **2005**, *26*, 1389–1392. [[CrossRef](#)]
- Ma, C.H.; Zhu, C.Q.; Liu, H.F.; Cui, X.; Wang, T.M.; Jiang, K.F.; Yi, M.X. State-of-the-Art Review of Research on the Particle Shape of Soil. *Rock Soil Mech.* **2021**, *42*, 2041–2058. [[CrossRef](#)]
- Wang, X.Z.; Wang, X.; Liu, H.F.; Meng, Q.S.; Zhu, C.Q. Field Test Study of Engineering Behaviors of Coral Reef Foundation. *Rock Soil Mech.* **2017**, *38*, 2065–2070+2079. [[CrossRef](#)]

10. Qing, Y.; Yao, T.; Wang, R.; Zhu, C.Q.; Meng, Q.S. Particle Breakage-Based Analysis of Deformation Law of Calcareous Sediments under High-Pressure Consolidation. *Rock Soil Mech.* **2014**, *35*, 3123–3128. [[CrossRef](#)]
11. Wang, X.Z.; Wang, X.; Weng, Y.L.; Lv, S.Z.; Yan, K.; Zhu, C.Q. Characteristics of Dry Density of Calcareous Sand and Its Testing Methods. *Rock Soil Mech.* **2016**, *37*, 316–322. [[CrossRef](#)]
12. Varadarajan, A.; Sharma, K.G.; Venkatachalam, K.; Gupta, A.K. Testing and Modeling Two Rockfill Materials. *J. Geotech. Geoenviron. Eng.* **2003**, *129*, 206–218. [[CrossRef](#)]
13. Xiao, Y.; Liu, H.L.; Ding, X.M.; Chen, Y.M.; Jiang, J.S.; Zhang, W.G. Influence of Particle Breakage on Critical State Line of Rockfill Material. *Int. J. Geomech.* **2016**, *16*, 04015031. [[CrossRef](#)]
14. Konrad, J.-M.; Salami, Y. Particle Breakage in Granular Materials—A Conceptual Framework. *Can. Geotech. J.* **2018**, *55*, 710–719. [[CrossRef](#)]
15. Lade, P.V.; Yamamuro, J.A.; Bopp, P.A. Significance of Particle Crushing in Granular Materials. *J. Geotech. Eng.* **1996**, *122*, 309–316. [[CrossRef](#)]
16. Wang, Y.; Santosh, M.; Luo, Z.H.; Hao, J.H. Large Igneous Provinces Linked to Supercontinent Assembly. *J. Geodyn.* **2015**, *85*, 1–10. [[CrossRef](#)]
17. Jia, Y.F.; Wang, B.S.; Chi, S.C. Particle breakage of rockfill during triaxial tests. *Chin. J. Geotech. Eng.* **2015**, *37*, 1692–1697. [[CrossRef](#)]
18. Yu, F.W. Characteristics of Particle Breakage of Sand in Triaxial Shear. *Powder Technol.* **2017**, *320*, 656–667. [[CrossRef](#)]
19. Liu, S.H.; Mao, H.Y.; Wang, Y.S.; Weng, L.P. Experimental Study on Crushable Coarse Granular Materials during Monotonic Simple Shear Tests. *Geomech. Eng.* **2018**, *15*, 687–694. [[CrossRef](#)]
20. Wu, Y.Q.; Tahmasebi, P.; Lin, C.Y.; Zahid, M.A.; Dong, C.M.; Golab, A.N.; Ren, L.H. A Comprehensive Study on Geometric, Topological and Fractal Characterizations of Pore Systems in Low-Permeability Reservoirs Based on SEM, MICP, NMR, and X-ray CT Experiments. *Mar. Pet. Geol.* **2019**, *103*, 12–28. [[CrossRef](#)]
21. Weibull, W. A Statistical Distribution Function of Wide Applicability. *J. Appl. Mech.* **1951**, *18*, 293–297. [[CrossRef](#)]
22. Coop, M.R.; Sorensen, K.K.; Freitas, T.B.; Georgoutsos, G. Particle Breakage during Shearing of a Carbonate Sand. *Geotechnique* **2004**, *54*, 157–163. [[CrossRef](#)]
23. Zhang, J.M.; Zhang, L.; Jiang, G.S.; Wang, R. Research on Particle Crushing of Calcareous Sands under Triaxial Shear. *Rock Soil Mech.* **2008**, *29*, 2789–2793. [[CrossRef](#)]
24. Yan, C.P.; Long, Z.L.; Zhou, Y.C.; Kuang, D.M.; Chen, J.M. Investigation on the Effects of Confining Pressure and Particle Size of Shear Characteristics of Calcareous Sand. *Rock Soil Mech.* **2020**, *41*, 581–591+634. [[CrossRef](#)]
25. Toyota, H.; Susami, A.; Takada, S. Anisotropy of Undrained Shear Strength Induced by K0 Consolidation and Swelling in Cohesive Soils. *Int. J. Geomech.* **2014**, *14*, 04014019. [[CrossRef](#)]
26. Hwang, J.; Dewoolkar, M.; Ko, H.-Y. Stability Analysis of Two-Dimensional Excavated Slopes Considering Strength Anisotropy. *Can. Geotech. J.* **2002**, *39*, 1026–1038. [[CrossRef](#)]
27. Coccia, C.R.; McCartney, J. A Thermo-Hydro-Mechanical True Triaxial Cell for Evaluation of the Impact of Anisotropy on Thermally Induced Volume Changes in Soils. *Geotech. Test. J.* **2012**, *35*, 227–237. [[CrossRef](#)]
28. Pan, K.; Yang, Z.X.; Xu, T.T. Impact of Static Preshearing on Undrained Anisotropy and Shear Characteristics of Sand. *Int. J. Geomech.* **2018**, *18*, 04018162. [[CrossRef](#)]
29. He, S.H.; Goudarzy, M.; Ding, Z.; Sun, Y.F. Strength, Deformation, and Particle Breakage Behavior of Calcareous Sand: Role of Anisotropic Consolidation. *J. Geotech. Geoenvironmental Eng.* **2023**, *149*, 04023002. [[CrossRef](#)]
30. Cundall, P.A.; Strack, O.D.L. A Discrete Numerical Model for Granular Assemblies. *Geotechnique* **1979**, *29*, 47–65. [[CrossRef](#)]
31. Zhang, T.; Wu, J. Discriminative Frequency Filter Banks Learning with Neural Networks. *Eurasip J. Audio Speech Music Process.* **2019**, *2019*, 1. [[CrossRef](#)]
32. Dahal, B.; Mishra, D. Discrete Element Modeling of Permanent Deformation Accumulation in Railroad Ballast Considering Particle Breakage. *Front. Built Environ.* **2020**, *5*, 145. [[CrossRef](#)]
33. Afshar, T.; Disfani, M.M.; Arulrajah, A.; Narsilio, G.A.; Emam, S. Impact of Particle Shape on Breakage of Recycled Construction and Demolition Aggregates. *Powder Technol.* **2017**, *308*, 1–12. [[CrossRef](#)]
34. Zhang, T.; Zhang, C.; Zou, J.; Wang, B.; Song, F.; Yang, W. DEM Exploration of the Effect of Particle Shape on Particle Breakage in Granular Assemblies. *Comput. Geotech.* **2020**, *122*, 103542. [[CrossRef](#)]
35. Ueda, T.; Matsushima, T.; Yamada, Y. DEM Simulation on the One-Dimensional Compression Behavior of Various Shaped Crushable Granular Materials. *Granul. Matter* **2013**, *15*, 675–684. [[CrossRef](#)]
36. McDowell, G.R.; Hariireche, O. Discrete Element Modelling of Soil Particle Fracture. *Geotechnique* **2002**, *52*, 131–135. [[CrossRef](#)]
37. Qu, T.; Feng, Y.T.; Wang, Y.; Wang, M. Discrete Element Modelling of Flexible Membrane Boundaries for Triaxial Tests. *Comput. Geotech.* **2019**, *115*, 103154. [[CrossRef](#)]
38. Liu, Y.; Liu, H.; Mao, H. DEM Investigation of the Effect of Intermediate Principle Stress on Particle Breakage of Granular Materials. *Comput. Geotech.* **2017**, *84*, 58–67. [[CrossRef](#)]
39. Smilauer, V.; Angelidakis, V.; Catalano, E.; Caulk, R.; Chareyre, B.; Chevremont, W.; Dorofeenko, S.; Duriez, J.; Dyck, N.; Elias, J.; et al. Yade Documentation. *arXiv* **2023**, arXiv:2301.00611.
40. Gao, Y.; Shi, T.; Yuan, Q.; Sun, K. The Creep Characteristics and Related Evolution of Particle Morphology for Calcareous Sand. *Powder Technol.* **2024**, *431*, 119077. [[CrossRef](#)]

41. Gladkyy, A.; Kuna, M. DEM Simulation of Polyhedral Particle Cracking Using a Combined Mohr–Coulomb–Weibull Failure Criterion. *Granul. Matter* **2017**, *19*, 41. [[CrossRef](#)]
42. Brzeziński, K.; Gladky, A. Clump Breakage Algorithm for DEM Simulation of Crushable Aggregates. *Tribol. Int.* **2022**, *173*, 107661. [[CrossRef](#)]
43. Ciantia, M.O.; Arroyo, M.; Calvetti, F.; Gens, A. An Approach to Enhance Efficiency of DEM Modelling of Soils with Crushable Grains. *Geotechnique* **2015**, *65*, 91–110. [[CrossRef](#)]
44. Zhang, K.; Zhang, S.; Teng, J.; Sheng, D. 3D Numerical Simulation of Particle Breakage Using Discrete Element Method. *Rock Soil Mech.* **2017**, *38*, 2119–2127. [[CrossRef](#)]
45. Zhao, F.; Chi, S. A Simulation Method for Particle Breakage with Random Fragment Size Based on Discrete Element Method. *J. Northeast. Univ. Nat. Sci.* **2023**, *44*, 408–414.
46. Benjamin, M. An Investigation of Strain Localization in Cemented Sands and Mechanisms of Stiffness Anisotropy Using the Dem Simulations—Rare & Special e-Zone. Master's Thesis, The Hong Kong University of Science and Technology, Hong Kong, China, 2007.
47. Stokoe, K.; Lee, S.; Knox, D.P. Shear Moduli Measurements under True Triaxial Stresses. In *Advances in the Art of Testing Soils Under Cyclic Conditions*; ASCE: Reston, VA, USA, 1985.
48. Stokoe, K.H.I.; Hwang, S.K.; Lee, J.N.K.; Andrus, R.D. Effects of Various Parameters on the Stiffness and Damping of Soils at Small to Medium Strains. In *Pre-Failure Deformation of Geomaterials, Proceedings of the International Symposium on Pre-Failure Deformation Characteristics of Geomaterials, Sapporo, Japan, 12 September 1994*; CRC Press: Boca Raton, FL, USA, 1994; pp. 785–816.
49. Stokoe, K.H.I.; Lee, J.N.K.; Lee, S.H.H. Characterization of Soil in Calibration Chambers with Seismic Waves. In *Calibration Chamber Testing, Proceedings of the First International Symposium on Calibration Chamber Testing/ISOCCT1, Potsdam, NY, USA, 28–29 June 1991*; Elsevier: Amsterdam, The Netherlands, 1991; pp. 363–376.
50. Ismail, M.A.; Sharma, S.S.; Fahey, M. A Small True Triaxial Apparatus with Wave Velocity Measurement. *Geotech. Test. J.* **2005**, *28*, 113–122. [[CrossRef](#)]
51. Chaney, R.; Demars, K.; Fioravante, V.; Capoferri, R. On the Use of Multi-Directional Piezoelectric Transducers in Triaxial Testing. *Geotech. Test. J.* **2001**, *24*, 243. [[CrossRef](#)]
52. Radjai, F.; Wolf, D.E.; Jean, M.; Moreau, J.-J. Bimodal Character of Stress Transmission in Granular Packings. *Phys. Rev. Lett.* **1998**, *80*, 61–64. [[CrossRef](#)]
53. Satake, M. Fabric Tensor in Granular Materials. In *Deformation and Failure of Granular Materials, Proceedings of the IUTAM-Conference on Deformation and Failure of Granular Materials, Delft, The Netherlands, 31 August–3 September 1982*; Elsevier: Amsterdam, The Netherlands, 1982; pp. 63–68.
54. Sitharam, T.G.; Vinod, J.S.; Ravishankar, B.V. Post-Liquefaction Undrained Monotonic Behaviour of Sands: Experiments and DEM Simulations. *Géotechnique* **2009**, *59*, 739–749. [[CrossRef](#)]
55. Cai, Z.; Chen, Y.; Zhu, X.; Tang, Y. Influences of Gradation on Particle Breakage and Deformation Characteristics of Coral Sand. *Chin. J. Geotech. Eng.* **2023**, *45*, 661–670.
56. Russell, A.R.; Muir Wood, D. Point Load Tests and Strength Measurements for Brittle Spheres. *Int. J. Rock Mech. Min. Sci.* **2009**, *46*, 272–280. [[CrossRef](#)]
57. Gao, Y.; Yu, J.Y.; Wang, Y.B.; Li, W.L.; Shi, T.G. Breakage Effect of Calcareous Sand on Pile Tip Resistance and the Surrounding Soil Stress. *Energy Rep.* **2022**, *8*, 183–190. [[CrossRef](#)]
58. Chen, Q.; Gao, Y.; Yuan, Q.; Yu, J.Y. Microstructural Response during Shearing Process of Dense Sand. *Water Resources Hydropower Eng.* **2021**, *52*, 178–187. [[CrossRef](#)]

Disclaimer/Publisher's Note: The statements, opinions and data contained in all publications are solely those of the individual author(s) and contributor(s) and not of MDPI and/or the editor(s). MDPI and/or the editor(s) disclaim responsibility for any injury to people or property resulting from any ideas, methods, instructions or products referred to in the content.